

# Adaptive beamforming for array signal processing in aeroacoustic measurements

Xun Huang<sup>a)</sup>

*State Key Laboratory of Turbulence and Complex Systems, Department of Aeronautics and Astronautics, Peking University, Beijing, 100871, China*

Long Bai and Igor Vinogradov

*Department of Mechanics and Aerospace Engineering, Peking University, Beijing, 100871, China*

Edward Peers

*Department of Aeronautics and Astronautics, Peking University, Beijing, 100871, China*

(Received 15 June 2011; revised 4 January 2012; accepted 9 January 2012)

Phased microphone arrays have become an important tool in the localization of noise sources for aeroacoustic applications. In most practical aerospace cases the conventional beamforming algorithm of the delay-and-sum type has been adopted. Conventional beamforming cannot take advantage of knowledge of the noise field, and thus has poorer resolution in the presence of noise and interference. Adaptive beamforming has been used for more than three decades to address these issues and has already achieved various degrees of success in areas of communication and sonar. In this work an adaptive beamforming algorithm designed specifically for aeroacoustic applications is discussed and applied to practical experimental data. It shows that the adaptive beamforming method could save significant amounts of post-processing time for a deconvolution method. For example, the adaptive beamforming method is able to reduce the DAMAS computation time by at least 60% for the practical case considered in this work. Therefore, adaptive beamforming can be considered as a promising signal processing method for aeroacoustic measurements.

© 2012 Acoustical Society of America. [DOI: 10.1121/1.3682041]

PACS number(s): 43.60.Fg, 43.60.Jn, 43.28.Ra [DKW]

Pages: 2152–2161

## I. INTRODUCTION

Beamforming techniques with microphone arrays<sup>1–3</sup> are increasingly being used in the aerospace industry<sup>4,5</sup> to localize the distribution of airframe noise to allow the development of efficient noise control strategies.<sup>6</sup> Airframe noise is particularly evident during landing when the engines operate at a low power setting<sup>7</sup> and the high lift devices and landing gear are deployed. Generally, airframe noise is produced by a fluid–structure interaction of aerodynamic surfaces and the surrounding turbulent flow.<sup>8</sup> Scaled models of airframe components, which include high lift devices, landing gear, wheel wells, and sharp trailing edges, have recently been tested in wind tunnels and anechoic chambers to investigate aeroacoustic related flow mechanisms and localize noise source distributions using acoustic imaging techniques.<sup>9</sup>

Beamforming is a technique that uses a sensor array to visualize the location of a signal of interest.<sup>10</sup> Various applications can be found in radar, sonar, communications, and medical imaging. Aeroacoustic measurements are, to some extent, challenging for beamforming because of the poor signal-to-noise ratio and multipath effects in a traditional aerodynamic testing facility.<sup>5</sup> To address these issues, a test facility has to be modified specifically to reduce background noise and to mitigate wall reflections.<sup>11,12</sup> Particular attention has also been paid to array design in order to reduce the

detrimental effect of the background noise. More design details can be found in Refs. 4, 13, and 14. On the other hand, although numerous beamforming methods have been proposed in the last three decades, the conventional beamforming method<sup>10</sup> with the delay-and-sum approach and its variants<sup>3,13,15</sup> are still the dominant technique used for aeroacoustic measurements.

From the perspective of signal processing, an acoustic imaging process can be regarded as a convolution between the array frequency responses and acoustic sources of interest. The frequency response of the conventional beamforming method has a wide main lobe and high side lobe peaks, which masks the signal of interest through convolution, leading to the well-known limited resolution problem. To address this issue, several different deconvolution algorithms<sup>16–21</sup> have recently been proposed to post-process conventional beamforming results in order to restore the signals of interest.

Nowadays the conventional beamformer with the delay-and-sum approach is rarely used in sonar, radar, and communication applications, for which the method was initially developed. An alternative method, adaptive beamforming, or the so-called Capon beamforming, has a much better resolution and interference rejection capability<sup>22</sup> and has been adopted as a de facto method in array signal processing. It is natural to expect that an adaptive beamformer could be helpful to pinpoint aeroacoustic noise sources more accurately and better minimize the convolution effects,<sup>5</sup> which, in turn, could produce array outputs of higher quality saving the computational efforts of the aforementioned deconvolution

<sup>a)</sup>Author to whom correspondence should be addressed. Electronic mail: huangxun@pku.edu.cn

methods. However, adaptive beamforming is quite sensitive to any perturbations and its performance can quickly deteriorate below an acceptable level, preventing the direct application of present adaptive beamforming methods for aeroacoustic measurements.

It is generally assumed that errors in array measurements are mainly from steering vectors,<sup>23</sup> which are determined by the relative distances between a signal of interest and the array microphones. More often than not, a steering vector deviates from the expected one. Installation of a microphone array on a vibrating testing facility wall is partially responsible for this problem. Any mismatch in steering vector leads to significant computational error due to the sensitive nature of adaptive beamforming. The steering vector can therefore be regarded within a predefined uncertainty ellipsoid and a robust beamformer<sup>24</sup> can be consequently designed to maintain an acceptable accuracy within the complete uncertainty ellipsoid<sup>25</sup> (see references therein for more details of the approach). Diagonal loading is the other popular approach to improve the robustness of an adaptive beamformer. This method has been adopted in the current work for its simplicity of implementation. The same approach has already been used in previous aeroacoustic measurements.<sup>5,26</sup> It can be seen that the performance of diagonal loading depends on a suitable choice of loading parameter. An iterative procedure has been adopted in this work to straightforwardly find an appropriate value of the loading parameter in practical aeroacoustic tests.

In previous work,<sup>5,26</sup> adaptive beamforming for aeroacoustics has only been applied for numerical benchmark cases or idealized cases with speakers as experimental noise sources. To the best of our knowledge, there is no literature dealing with development and/or application of adaptive beamforming for practical aeroacoustic setups. Because the only way to validate an algorithm is to apply it for practical applications, the main contribution of this work fills the gap, using an adaptive beamforming for one of the landing gear components. First, the adaptive beamforming algorithm developed specifically for aeroacoustics is proposed in Sec. II. The experimental setup of the aeroacoustic test is summarized in Sec. III and the related acoustic imaging results are reviewed in Sec. IV. Advantages and shortcomings of adaptive beamforming for aeroacoustics are discussed in Sec. V.

## II. FORMULATIONS

### A. Sound field model

The notations that generally appear in the literature<sup>5,23</sup> are adopted in the following. Given a microphone array with  $M$  microphones, the output  $\mathbf{x}(t)$  denotes time domain measurements of microphones,  $x \in \mathbb{R}^{M \times 1}$  and  $t$  denotes time. For a single signal of interest  $s(t) \in \mathbb{R}^1$  in a free sound propagation space, using Green's function for the wave equation in a free space, we can have

$$\mathbf{x}(t) = \frac{1}{4\pi\mathbf{r}} s(t - \tau), \quad \tau = \frac{\mathbf{r}}{C}, \quad (1)$$

where  $C$  is the speed of sound,  $r \in \mathbb{R}^{M \times 1}$  are the distances between the signal of interest  $s$  and microphones, and  $\tau$  is the related sound propagation time delay between  $s$  and the microphones. For most aeroacoustic applications, beamforming is generally conducted in the frequency domain.<sup>18</sup> The frequency domain version of Eq. (1) is

$$\mathbf{X}(j\omega) = \frac{1}{4\pi\mathbf{r}} S(j\omega) e^{-j\omega\tau} = \mathbf{a}_0(\mathbf{r}, j\omega) S(j\omega), \quad (2)$$

where  $j = \sqrt{-1}$ ,  $\mathbf{a}_0$  is the steering vector,  $\omega$  is angular frequency,  $(j\omega)$  and  $(\mathbf{r}, j\omega)$  can be omitted for brevity,  $\mathbf{X}$  and  $S$  are counterparts in the frequency domain, and we can simply write Eq. (2) as  $\mathbf{X} = \mathbf{a}_0 S$ .

The situation becomes more complex for a practical case, for which the array output vector can be represented as

$$\mathbf{X} = \mathbf{a}_0 S + \mathbf{I} + \mathbf{N}, \quad (3)$$

where  $\mathbf{I}$  is the interference from coherent signals and/or reflections and  $\mathbf{N}$  denotes the collective error from facility background noise and sensor noise. It is worthwhile to note that the signal of interest ( $S$ ), interference ( $\mathbf{I}$ ), and noise ( $\mathbf{N}$ ) are of zero-mean signal waveforms, and  $S$  and  $\mathbf{N}$  are generally assumed statistically independent for simplicity.

Let  $\mathbf{R}_X$ ,  $\mathbf{R}_{IN}$ , and  $\mathbf{R}_S$  denote the  $M \times M$  theoretical covariance matrix (also known as the cross spectrum matrix or cross-spectral density matrix) of the array output vector and interference-plus-noise covariance and signal of interest covariance matrices, respectively; and then we have

$$\mathbf{R}_X = E\{\mathbf{X}\mathbf{X}^*\}, \quad (4)$$

$$\mathbf{R}_{IN} = E\{(\mathbf{I} + \mathbf{N})(\mathbf{I} + \mathbf{N})^*\}, \quad (5)$$

$$\mathbf{R}_S = E\{\alpha^2 \mathbf{a}_0 \mathbf{a}_0^*\} = \mathbf{R}_X - \mathbf{R}_{IN}, \quad \text{if } E\{\mathbf{X}(\mathbf{I} + \mathbf{N})^*\} = 0, \quad (6)$$

where  $(\cdot)^*$  stands for conjugate transpose,  $E\{\cdot\}$  denotes the statistical expectation, and  $\sigma^2 = E\{|S|^2\}$  is the variance of  $S$ . In practical aeroacoustic measurements,  $\mathbf{N}$  denotes background noise that can be measured separately without the presence of any test model, which is a practice generally adopted in aeroacoustic experiments.<sup>4,9,17,18</sup> The measurements of  $\mathbf{X}$  can be conducted thereafter with the placement of a test model within the test section. The statistics of the signal of interest  $\sigma^2$  can be subsequently estimated and a suitable beamforming method with a narrow main lobe and small side lobes can reduce interference from unknown  $\mathbf{I}$ . The assumption of  $E\{\mathbf{X}(\mathbf{I} + \mathbf{N})^*\} = 0$  suggests that no correlation between the signal of interest and the interference plus the facility background noise. The assumption is normally valid in most aeroacoustic experiments and therefore has been widely adopted.<sup>17,18</sup> For the correlated case, a so-called observer-based beamforming method has been proposed in the literature<sup>13,27,28</sup> to address the issue.

In practical applications, the covariance matrix  $\mathbf{R}$  is approximated by sample covariance matrices, which are constructed based on array samples  $\mathbf{X}$  and  $\mathbf{N}$ . We can have

$$\hat{\mathbf{R}}_X \approx \frac{1}{K} \sum_{k=1}^K \mathbf{X}\mathbf{X}^*, \quad (7)$$

where the caret denotes approximations and  $K$  is the number of sampling blocks which is preferably a large number (e.g., 100 was empirically chosen in experiments), compared to the period of signal of interest, for statistical confidence. In addition,  $\mathbf{R}_{IN}$  has to be approximated in the following form as the interference  $\mathbf{I}$  is largely unknown:

$$\hat{\mathbf{R}}_{IN} \approx \frac{1}{K} \sum_{k=1}^K \mathbf{N}\mathbf{N}^*. \quad (8)$$

And finally the approximation for  $\mathbf{R}_S$  is

$$\hat{\mathbf{R}}_S \approx \hat{\mathbf{R}}_X - \hat{\mathbf{R}}_{IN}. \quad (9)$$

## B. Conventional beamforming

A narrowband beamformer output for each frequency bin of interest can be written as

$$\mathbf{Y} = \mathbf{W}^* \mathbf{X}, \quad (10)$$

where  $\mathbf{Y}$  is the beamformer output and  $\mathbf{W} \in C^{M \times 1}$  is the beamformer weight vector. For the conventional beamformer of delay-and-sum type, the beamformer weight vector is obtained by minimizing the approximation error<sup>10</sup>

$$\min_{\mathbf{w}} \mathbf{W}^* \mathbf{W} \text{ subject to } \mathbf{W}^* \mathbf{a}_0 = 1. \quad (11)$$

It is easy to see that the solution is  $\mathbf{W}_{opt} = (\mathbf{a}_0 \mathbf{a}_0^*)^{-1} \mathbf{a}_0$  yielding the following estimation of  $\sigma^2$ :

$$\hat{\sigma}^2 = \mathbf{W}_{opt}^* \hat{\mathbf{R}}_S \mathbf{W}_{opt} = \mathbf{a}_0^* (\mathbf{a}_0 \mathbf{a}_0^*)^{-1} \hat{\mathbf{R}}_S (\mathbf{a}_0 \mathbf{a}_0^*)^{-1} \mathbf{a}_0, \quad (12)$$

where  $\hat{\mathbf{R}}_S$  can be approximated with Eq. (9) in experiments and  $\mathbf{a}_0$  can be obtained with array geometry and experimental setup details.

## C. Adaptive beamforming

The fundamental idea behind Capon beamforming is to obtain  $\mathbf{W}_{opt}$  through maximizing the signal-to-interference-plus ratio (SINR),

$$\text{SINR} = \frac{\mathbf{W}^* \mathbf{R}_S \mathbf{W}}{\mathbf{W}^* \mathbf{R}_{IN} \mathbf{W}}, \quad (13)$$

and maintaining distortionless response toward the direction of the signal of interest.<sup>23,29</sup> In other words, the expected effect of the noise and interferences should be minimized, thus leading to the following linearly constrained quadratic problem:<sup>30</sup>

$$\min_{\mathbf{W}} \mathbf{W}^* \mathbf{R}_{IN} \mathbf{W} \text{ subject to } \mathbf{W}^* \mathbf{a}_0 = 1, \quad (14)$$

The solution can be obtained with a Lagrange multiplier,<sup>10</sup> i.e.,  $\mathbf{W}_{opt} = \alpha \mathbf{R}_{IN}^{-1} \mathbf{a}_0$ , where  $\alpha$  is a constant that equals  $(\mathbf{a}_0^* \mathbf{R}_{IN}^{-1} \mathbf{a}_0)^{-1}$ . In practical aeroacoustic applications the covariance matrix  $\mathbf{R}_{IN}$  is unavailable and has to be approximated by the sampling covariance matrix  $\hat{\mathbf{R}}_X$ . We can have

$$\hat{\sigma}^2 = \hat{\mathbf{W}}_{opt}^* \hat{\mathbf{R}}_S \hat{\mathbf{W}}_{opt}, \quad (15)$$

where  $\hat{\mathbf{W}}_{opt} = \hat{\mathbf{R}}_X^{-1} \mathbf{a}_0 / \mathbf{a}_0^* \hat{\mathbf{R}}_X^{-1} \mathbf{a}_0$  and  $\hat{\mathbf{R}}_S$  can be obtained using Eq. (9). It is worthwhile to mention that Eq. (15) is different from the classical form of adaptive beamforming,

$$\hat{\sigma}^2 = \hat{\mathbf{W}}_{opt}^* \hat{\mathbf{R}}_S \hat{\mathbf{W}}_{opt}, \quad (16)$$

where  $\hat{\mathbf{W}}_{opt}$  is the same as that in Eq. (15), whose solutions contain both background noise and the desired signal. Hence, Eq. (16) is not adopted in this work. In addition, the covariance matrix of the desired signal  $\hat{\mathbf{R}}_X$  and the noise  $\hat{\mathbf{R}}_{IN}$  can be approximated using Eqs. (8) and (9), respectively. One could also propose another alternative adaptive beamforming algorithm as shown in

$$\hat{\sigma}^2 = \hat{\mathbf{W}}_{opt}^* \hat{\mathbf{R}}_S \hat{\mathbf{W}}_{opt}, \quad (17)$$

where  $\hat{\mathbf{W}}_{opt} = \hat{\mathbf{R}}_{IN}^{-1} \mathbf{a}_0 / \mathbf{a}_0^* \hat{\mathbf{R}}_{IN}^{-1} \mathbf{a}_0$ . In this work we found that this algorithm fails to generate satisfactory results for practical data. The potential reason could be mismatches in background noise covariance matrices. That is,  $\hat{\mathbf{R}}_{IN}$  in Eq. (17) is obtained without the presence of any test model. The installation of a test model, however, could alter the background noise covariance matrix. As a result, Eq. (15) is adopted in this paper for adaptive beamforming implementation.

It is worthwhile to emphasize that the method [Eq. (14)] was originally proposed for rank-one signal (point source) cases. However, the number of discrete noise sources distributed in a practical aeroacoustic case could be larger than the number of array microphones. As a result,  $\hat{\mathbf{R}}_X$  could have a full rank. The direct application of Eq. (15) [the solution of Eq. (14)] for acoustic imaging could lead to questionable results. Hence, specific modifications of  $\hat{\mathbf{R}}_X$  have to be conducted, the details of which can be found in Sec. IV.

## D. Robust adaptive beamforming

The main objective of this paper is to investigate the performance of adaptive beamforming in practical aeroacoustic applications. In previous work we have already demonstrated that conventional beamforming with a delay-and-sum approach is independent of sample data and has been successfully applied for various aeroacoustic cases.<sup>13,31,32</sup> In contrast, the adaptive beamforming method is well known for its great sensitivity to any mismatches, perturbations, and data errors. A systematic solution has been proposed to improve the robustness of adaptive beamforming with respect to any mismatches in steering vectors.<sup>23,25</sup> In this work the array is placed outside of the free stream and should have little mismatch in steering vector (detailed setup is given in the next section). It is therefore assumed that the main computational error of an adaptive beamformer should

come from the ill-conditioning of sample matrices. Regularization methods can be used to mitigate the ill-conditioning by adding a suitable constant to diagonal elements of sample matrices. This is the so-called diagonal loading technique, which is one of the most popular approaches for robust adaptive beamforming. The regularized problem can be described by

$$\min_{\mathbf{W}} \mathbf{W}^* \mathbf{R}_N \mathbf{W} + \epsilon \mathbf{W}^* \mathbf{W} \text{ subject to } \mathbf{W}^* \mathbf{a}_0 = 1, \quad (18)$$

where the diagonal loading factor  $\epsilon$  imposes a penalty to avoid an inappropriately large array vector  $\mathbf{W}$ . The diagonal loaded version of Eq. (15) is

$$\hat{\sigma}^2 = \hat{\mathbf{W}}_{\text{opt}}^* \hat{\mathbf{R}}_S \hat{\mathbf{W}}_{\text{opt}}, \quad (19)$$

where  $\hat{\mathbf{W}}_{\text{opt}} = (\hat{\mathbf{R}}_X + \epsilon \mathbf{I}_M)^{-1} \mathbf{a}_0 / \mathbf{a}_0^* (\hat{\mathbf{R}}_X + \epsilon \mathbf{I}_M)^{-1} \mathbf{a}_0$  and  $\mathbf{I}_M$  is the  $M \times M$  identity matrix. It is easy to see that the diagonal loading ensures the invertibility of the loaded matrix  $\hat{\mathbf{R}}_X + \epsilon \mathbf{I}_M$  regardless of whether  $\hat{\mathbf{R}}_X$  is ill-conditioned.

The choice of the diagonal loading factor  $\epsilon$  is somewhat ad hoc. Empirical criteria for  $\epsilon$  with respect to the so-called white noise gain parameter has been given previously.<sup>16</sup> The latter parameter depends on physical insights. For simplicity, an iterative procedure is used in this work to tune  $\epsilon$ , which is set to  $\lambda \max [\text{eig}(\hat{\mathbf{R}}_X)]$ ,  $\text{eig}(\cdot)$  denotes the eigenvalues of a matrix. The diagonal loading parameter  $\lambda$  can be iteratively chosen between 0.01 and 0.5. A smaller  $\lambda$  normally produces an image with better resolution, but the computation can fail due to numerical instability. The computational failure is determined by comparing the maximal sound pressure values. Once the difference between the classical beamforming result and the adaptive beamforming result exceeds a threshold (empirically set to 3 dB), the adaptive beamforming computation fails. The value of  $\lambda$  is thus improper and has to be enlarged. On the other hand, a larger  $\lambda$  generates a result similar to that of a conventional beamformer. This finding is understandable as a big  $\lambda$  leads to a heavy penalty  $\epsilon$  in the optimization in Eq. (19) that therefore approaches Eq. (11).

For the following practical case we found that the value of  $\lambda$  can be quickly determined within a couple of iterations. The diagonal loading approach is hence used in the rest of this paper for its simplicity of implementation. In summary the beamforming algorithm for a narrowband frequency range is conducted as follows:

- Step 1: Compute sample covariance matrices  $\hat{\mathbf{R}}_X$  and  $\hat{\mathbf{R}}_S$ , and compute eigenvalues of  $\hat{\mathbf{R}}_X$ .
- Step 2: Given an observed plane, which has  $N$  gridpoints, construct steering vector  $\mathbf{a}_0$  for each gridpoint.
- Step 3: Calculate the diagonal loading factor  $\epsilon$  with an initial guess of  $\lambda = 0.01$ .  $\epsilon = \lambda \max [\text{eig}(\hat{\mathbf{R}}_X)]$ .
- Step 4: Repeat the adaptive beamforming equation [Eq. (19)] at each of  $N$  gridpoints to produce the acoustic image.
- Step 5: Qualitative check. The whole computation is completed if the quality is satisfactory and no numerical instability appears. Otherwise double the value of  $\lambda$  and repeat steps 3–5.

## E. Deconvolution approach

Various deconvolution algorithms(16–21) have been proposed to post-process beamforming results. The deconvolution approach for the mapping of acoustic sources (DAMAS)<sup>17</sup> was adopted in this work. For convenience of readers, the fundamental idea behind DAMAS is briefly introduced in the following.

The DAMAS approach resolves an inverse problem,  $\mathbf{Z} = \mathbf{A}\mathbf{S}$ , where  $\mathbf{Z} \in \mathbb{C}^{N \times 1}$  are the  $N$  estimations of each gridpoint, using Eq. (12) or Eq. (19), respectively;  $\mathbf{S} \in \mathbb{C}^{N \times 1}$  represents sound sources at each gridpoint and  $\mathbf{A} \in \mathbb{C}^{N \times N}$  is formed by the steering vectors, relating  $\mathbf{Z}$  to  $\mathbf{S}$ . The acoustic images shown in this work have  $121 \times 121$  gridpoints and  $N = 14\,641$ . It is thus extremely difficult to calculate the inverse of  $\mathbf{A}$ . An iterative scheme has been proposed<sup>17</sup> to estimate  $\mathbf{S}$  from  $\mathbf{Z}$ , instead of the direct calculation of the inverse of  $\mathbf{A}$ . As a result, the resolution of acoustic images could be extensively improved. For brevity, details of the algorithms are omitted. The interested reader should refer to the literature.<sup>17</sup>

## III. EXPERIMENTAL APPARATUS

To test the performance, the above adaptive signal processing algorithm is applied for a practical aeroacoustic case. The experiments have been conducted in an anechoic chamber facility (9.15 m  $\times$  9.15 m  $\times$  7.32 m) at ISVR, University of Southampton. Figure 1 shows the complete setup. A nozzle (500 mm  $\times$  350 mm) connecting to a plenum chamber can produce a jet flow of  $U_\infty = 30$  m/s. An array with 56 electret microphones (Panasonic WM-60A) is placed on the ground. The sensitivity of each microphone is  $-45 \pm 5$  dBV/Pa. The frequency response (amplitude and phase) of each microphone is calibrated to a B&K 4189 microphone in order to reduce inherent amplitude and phase differences between array microphones. An airframe model representing a part of a landing gear was placed right above the microphone array. The coordinates shown in Fig. 1 are used throughout the rest of the paper. The coordinate origin is at the center of the link structure of the triangle shape. The center of the array is aligned with the origin, and the distance from the origin is 0.7 m.

Figure 2 shows a photograph of the experimental setup in the test section. Two endplates are used to hold the bluff

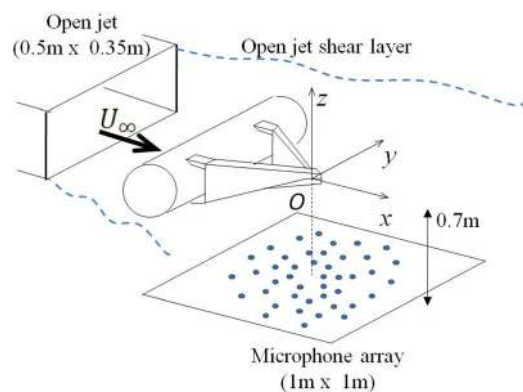


FIG. 1. (Color online) The illustration of the setup of experiment units (not to scale).



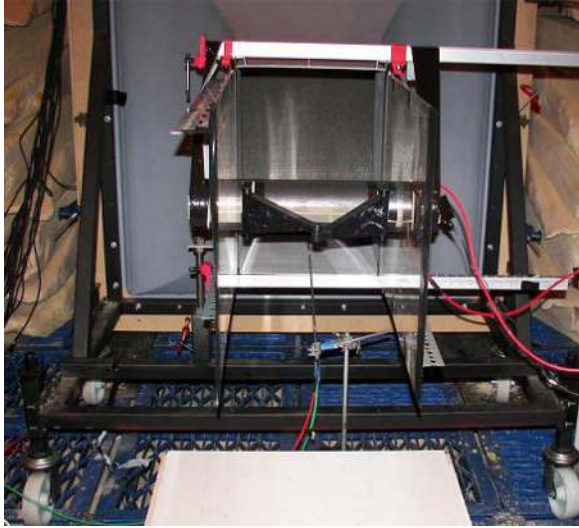


FIG. 2. (Color online) Overall system working in an anechoic chamber.

body model and maintain two-dimensional free stream flow in the open test section. A pitot tube is placed in front of the model to measure the free stream speed. The array is underneath the model. The shear layer correction based on Snell's law<sup>9</sup> is used in the beamforming signal processing as the array is placed outside of the testing flow. Measurements have also been conducted for a separate scenario without the presence of the model to approximate the facility background noise.

The size of the complete array is  $1\text{ m} \times 1\text{ m}$ . The effective diameter is  $0.64\text{ m}$ , within which microphones are deployed. The layout of microphones was designed for the particular purpose of reducing spatial aliasing.<sup>9</sup> The accu-

racy of the microphone locations is within  $1\text{ mm}$ . In addition, the array was placed outside of testing flow and firmly fastened to the ground to prevent any flow induced vibration, reducing the chance of any potential mismatch in the steering vectors of the array.

An NI PXI-1033 chassis with four 24 bit PXI-4496 cards has been used to simultaneously sample 56 channels of microphones at  $44\,000$  samples/s. Each data acquisition is operated through a band pass filter to remove the direct current part and to avoid high frequency aliasing. The data stream is cut into consecutive blocks, and each block contains 4096 samples for the discrete Fourier transform (DFT). The DFT amplitudes of each microphone are calibrated to a sound source of  $96\text{ dB}$  at  $1\text{ kHz}$ , and the decibel values are referenced to  $2 \times 10^{-5}\text{ Pa}$ .

#### IV. RESULTS AND DISCUSSION

A literature review shows that most previous work is focused on numerical examples. However, an application of an algorithm to experimental data is required to determine its applicability. In this work a practical aeroacoustic case involving a bluff body model is considered.

Figure 3 shows nondimensionalized acoustic image results at  $f = 5\text{ kHz}$ . The two horizontal lines in Fig. 3 represent the two endplates that help to maintain a better quality of test flow. The rest of the sketch illustrates the bluff body model. Two triangle-shaped bodies represent the components installed on the cylinder model, which are intentionally removed in Figs. 3(b)–3(d) to clearly show acoustic images. The whole bluff body is an idealized model of the main elements of an aircraft landing gear. The free stream direction

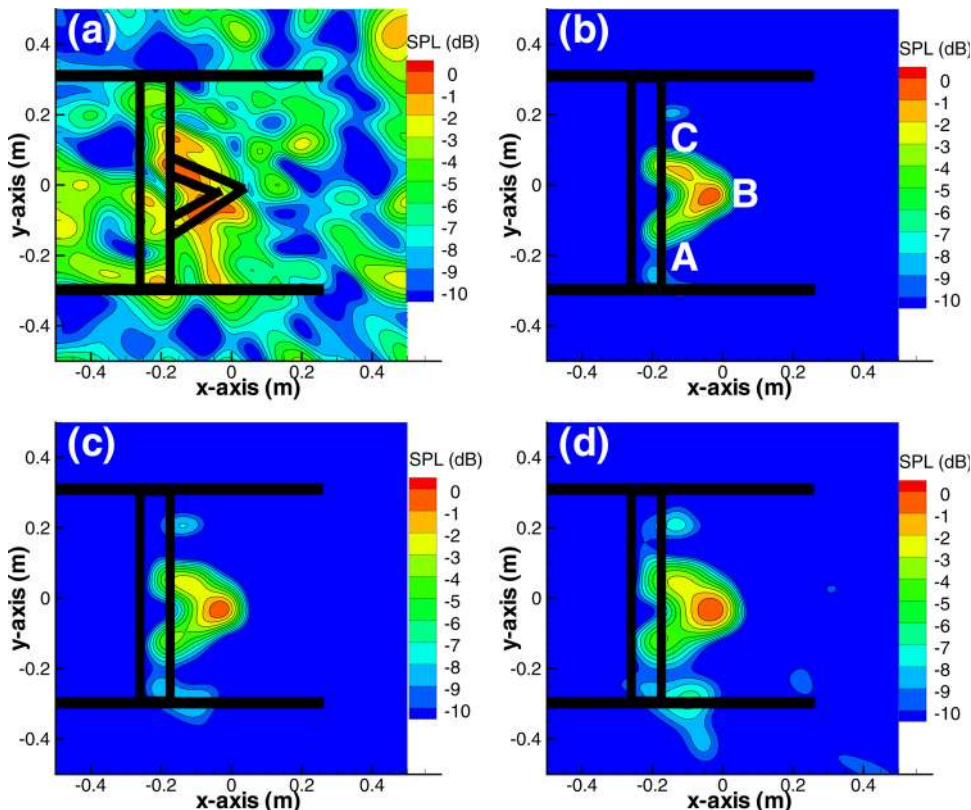


FIG. 3. (Color online) Acoustic image for the practical aeroacoustic case with a bluff body model, (a) the adaptive beamforming method [with Eq. (19) at  $\lambda = 0$ ], (b) the adaptive beamforming method [with Eq. (19) at  $\lambda = 0.1$ ], (c) the adaptive beamforming method [with Eq. (19) at  $\lambda = 0.5$ ], and (d) the conventional beamforming method [with Eq. (12)], respectively.  $f = 5\text{ kHz}$  and  $U_\infty = 30\text{ m/s}$ .

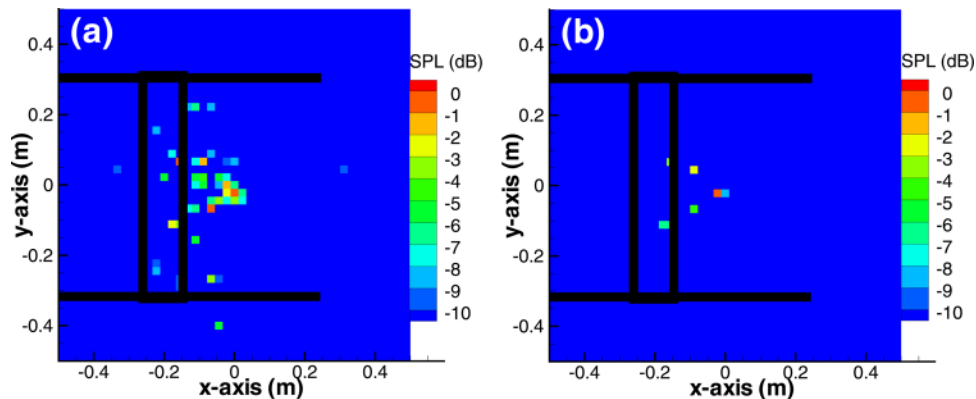


FIG. 4. (Color online) The DAMAS post-processing outcomes (1000 iterations) of the results of (a) conventional beamforming and (b) adaptive beamforming ( $\lambda = 0.5$ ) in Fig. 3, where  $f = 5$  kHz.

of the open jet is from the left to the right. All experiments have been conducted at  $U_\infty = 30 \pm 0.5$  m/s. The corresponding Reynolds number with respect to the cylinder diameter is in the order of  $10^5$ . The dominant flow-induced noise sources are located at the links [A–C in Fig. 3(b)]. More details related to the test model and related flow-induced noise mechanisms can be found in Ref. 31, whereas the attention of this paper is focused on the array signal processing method.

Figure 3(a) is the acoustic image obtained with Eq. (19) but without diagonal loading ( $\lambda$  and  $\epsilon$  equal 0). This figure contains chaotic acoustic imaging patterns with much lower sound pressure (see the upcoming Fig. 12), which suggests that the adaptive beamforming method without diagonal loading fails to identify dominant noise sources for practical aeroacoustic data. Any discrepancy in experimental measurements, such as multipath propagation, background noise or interference from coherent signals, and the mismatching of steering vectors, can lead to failure of adaptive beamformers.

Diagonal loading is used to address the issue, although the determination of a suitable diagonal loading parameter remains an open problem. For the case considered in this work,  $\lambda = 0.1$  and  $\lambda = 0.5$  have been tested and results are shown in Figs. 3(b) and 3(c), respectively. Both figures show that the background noise from the open jet has been rejected. Compared to the conventional beamforming results shown in Fig. 3(d), the positions and amplitudes of the dominant noise sources at the middle locations of the model agree well. Dynamic ranges of both adaptive beamforming and conventional beamforming results are quite similar, whereas the resolution has been improved. In addition, the resolution of Fig. 3(b) with  $\lambda = 0.1$  is somewhat better than that of Fig. 3(c) with  $\lambda = 0.5$ . In contrast the resolution of the conventional beamforming results is relatively low and some chaotic patterns can be found in Fig. 3(d), which are caused by the relatively high side lobes of the conventional beamforming method. It is worthwhile to point out that weights can be optimized (such as applying a window technique) to lower the side lobes. However, the width of the main lobe will be increased and the resolution will thus be sacrificed.

The adaptive beamforming method fails to improve resolution extensively for this practical case. This outcome answers the question frequently raised by signal processing experts: Why is adaptive beamforming so rarely used in aeroacoustic measurements? However, for its distinctive

side lobe suppression capability, the adaptive beamforming method can generate images with less spurious patterns, which could save huge amounts of post-processing time for a deconvolution method. DAMAS<sup>17</sup> has been conducted for the case to demonstrate the idea.

Figure 4 shows DAMAS results after 1000 iterations, which are initially post-processed on the conventional beamforming result [Fig. 3(d)] and the adaptive beamforming result [Fig. 3(b)], respectively. The noise sources in Fig. 4(a) fail to form a distinctive pattern and therefore show less physical insight. In contrast, the individual noise sources in Fig. 4(b) are clearly distributed along the triangle parts (excluded for clarity). This finding supports the above-mentioned statement regarding the adaptive beamforming method.

All beamforming methods introduced in this work were developed in MATLAB and computed on a desktop with an Intel i7 CPU (920 @ 2.67 GHz) and 8 GB memory. The code spent 110 s for the DAMAS method to finish 1000 iterations. It took an additional 30 000 iterations for Fig. 4(a) to achieve a pattern similar to that of Fig. 4(b). Hence, the adaptive beamforming method can help DAMAS quickly approach a reasonable source distribution. As a result, it is advantageous to consider adaptive beamforming in aeroacoustics. It is also worthwhile to point out that the conventional beamforming required 0.98 s to perform the calculation, whereas the adaptive beamforming required 1 s for the same case. These data are given here just for the readers' information as no particular optimization has been conducted for our code.

Acoustic images at various frequencies are shown in Figs. 5–8 to further illustrate the performance of beamforming methods. Figures 5(a) and 5(b) present acoustic image results at  $f = 2.5$  kHz using the conventional beamforming method and the adaptive beamforming method, respectively. The adaptive beamforming method is unable to realize a resolution advantage. However, again, DAMAS post-processing results can reveal the superior quality of the adaptive beamforming. Figure 6 shows the related results of 1000 DAMAS iterations. It can be seen that the DAMAS results for the conventional beamforming indicate a source distribution along the trailing triangle parts, whereas the DAMAS results for the adaptive beamforming identify the main noise sources at the links [A–C in Fig. 3(b)].

Figures 7(a) and 7(b) are acoustic images at  $f = 7.5$  kHz by conventional beamforming and adaptive beamforming,

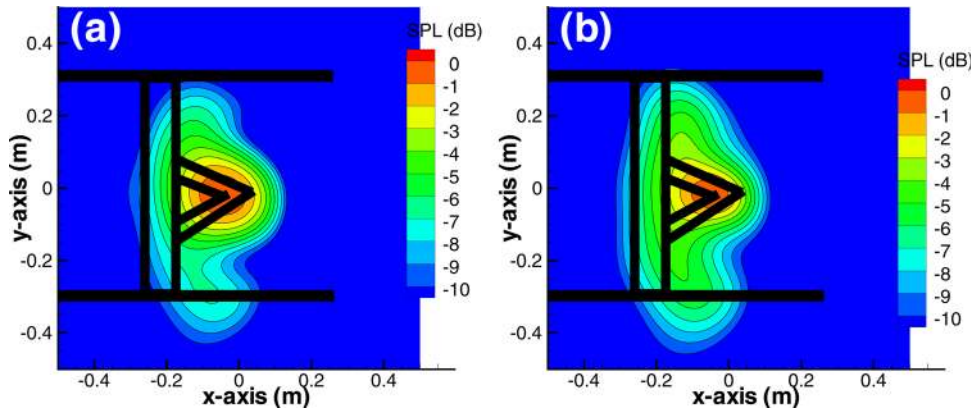


FIG. 5. (Color online) Acoustic image results of the practical aeroacoustic case, (a) the conventional beamforming method [with Eq. (12)] and (b) the adaptive beamforming method [with Eq. (19)] with diagonal loading at  $\lambda=0.5$ , where  $f=2.5$  kHz.

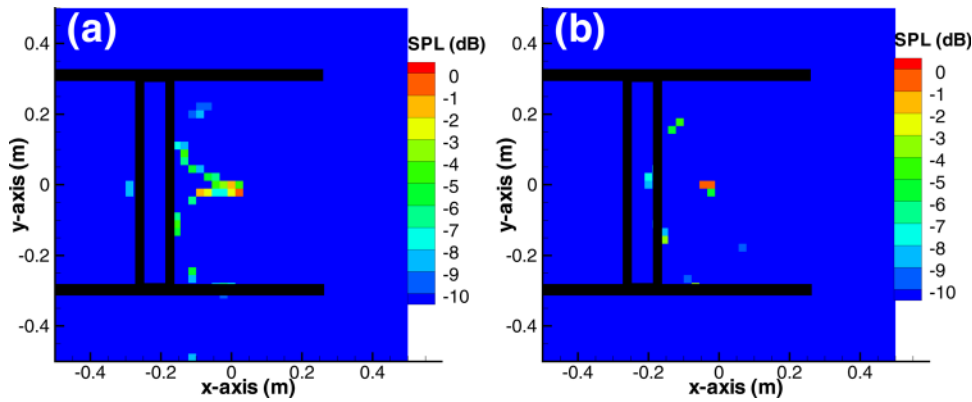


FIG. 6. (Color online) The DAMAS post-processing outcomes (1000 iterations) of the results of (a) conventional beamforming and (b) adaptive beamforming ( $\lambda=0.5$ ) in Fig. 5, where  $f=2.5$  kHz.

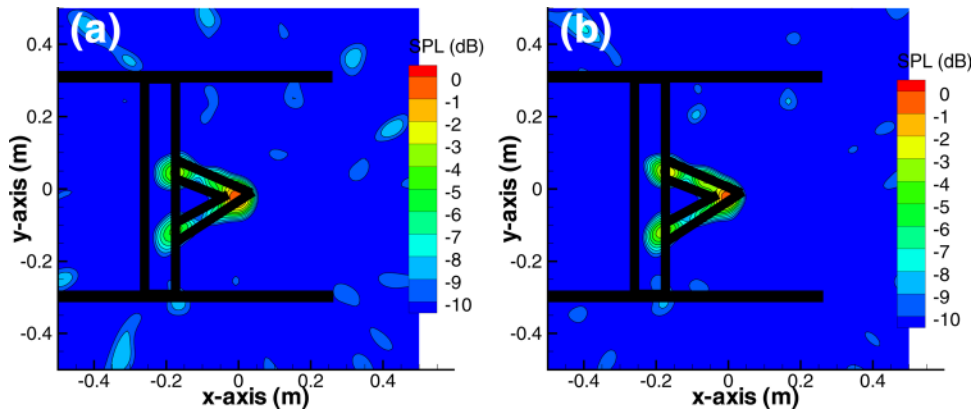


FIG. 7. (Color online) Acoustic image results of the practical aeroacoustic case, (a) the conventional beamforming method [with Eq. (12)] and (b) the adaptive beamforming method [with Eq. (19)] with diagonal loading at  $\lambda=0.5$ , where  $f=7.5$  kHz.

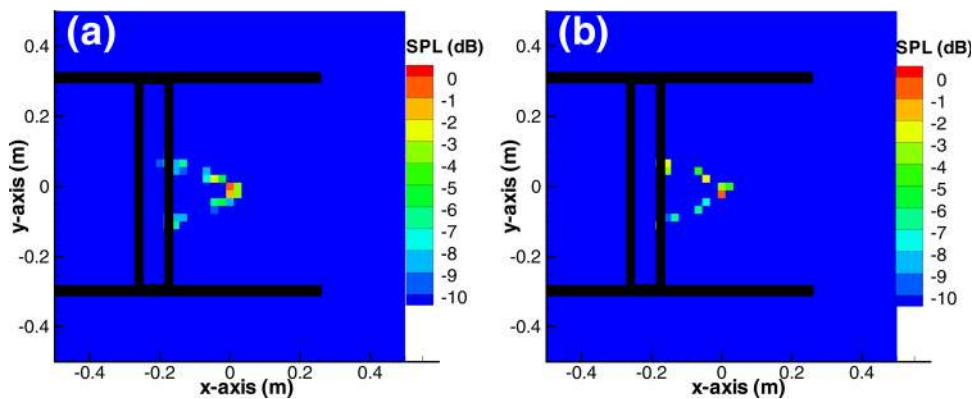


FIG. 8. (Color online) The DAMAS post-processing outcomes (1000 iterations) of the results of (a) conventional beamforming and (b) adaptive beamforming ( $\lambda=0.5$ ) in Fig. 7, where  $f=7.5$  kHz.



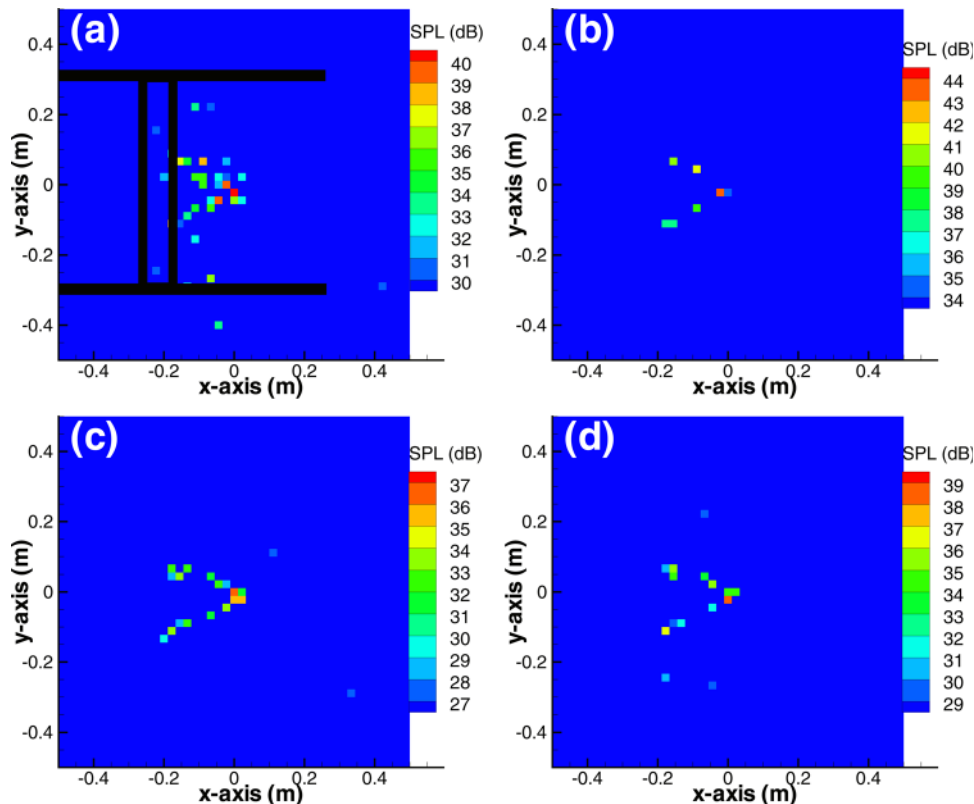


FIG. 9. (Color online) The DAMAS post-processing outcomes (10 000 iterations,  $\lambda=0.5$ ), where (a,b)  $f=5$  kHz and (c,d)  $f=7.5$  kHz; (a) and (c) are DAMAS results for the conventional beamforming solutions; (b) and (d) are DAMAS results for the adaptive beamforming solutions.

respectively. It can be seen that the acoustic image results at this higher frequency include some chaotic patterns, which are mainly caused by array sidelobes that are typically higher at higher frequencies for a given array design. The potential loss of sensitivity during the passage of the acoustic waves through the open jet shear layer could be the other cause. A high frequency sound suffers loss more than the low frequency sound, as the former's wavelength is more comparable to the characteristic width of the shear layer. Figure 8 shows the post-processing results of 1000 DAMAS iterations. It can be seen that adaptive beamforming helps to produce a DAMAS result with more distinctive noise distributions. It is also worthwhile to mention that a similar improvement is expected for other post-processing methods, such as CLEAN.<sup>18</sup> All results in Figs. 9–12 are shown in a normalized form. A calibration can be conducted to achieve absolute sound levels, which are shown in Fig. 9.

To quantitatively show the performance of different beamforming methods, sound pressure squared-mean values of the grid points within an integration region are summed up. Similar operations can be found in the literature.<sup>17</sup> The integration region is represented by a dashed rectangle in Fig. 10, which covers the dominant noise sources and is deliberately kept away from the two endplates, where the turbulent boundary flow affects acoustic measurements.

The total amount of the mean-squared values within the integration region is shown in Fig. 11. For the 5 kHz beamforming results [Fig. 11(a)], it can be seen that the total noise converges rapidly for the adaptive beamforming data. The total noise is within 1 dB after 10 DAMAS iterations and within 0.01 dB after 100 iterations. In contrast, the total noise converges much slower in the case of the conventional

beamforming data. The total noise converges within 1 dB after 15 iterations. However, after 300 iterations, the convergence speed slows down to less than 0.01 dB per 100 iterations. Convergence is still not achieved after 10 000 iterations (which is not shown here for brevity). Similar findings have been reported for low frequency cases in literature.<sup>17</sup> These two results suggest that the adaptive beamforming method used here can extensively reduce the required post-processing effort for DAMAS.

It has also been found that DAMAS results converge more quickly for high frequency cases.<sup>17</sup> The same experiments have been conducted for the 7.5 kHz case and the results are shown in Fig. 11(b). Once again, the adaptive

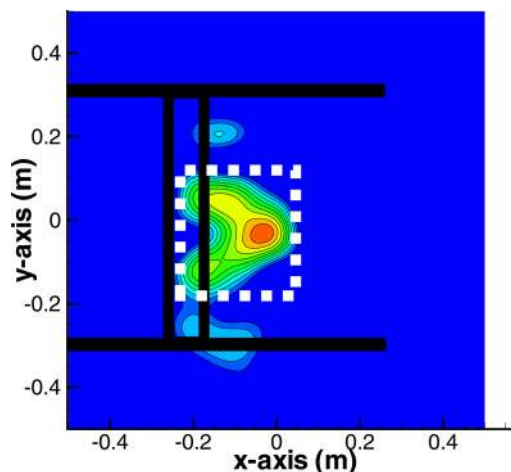


FIG. 10. (Color online) The mean-squared sound pressure values are summed within the dashed rectangular integration region.



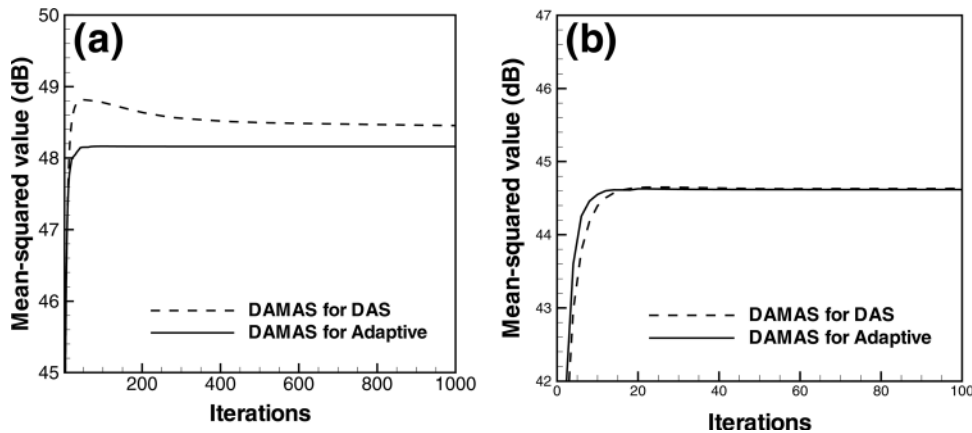


FIG. 11. The mean-squared sound pressure values for the DAMAS results of the conventional delay-and-sum (DAS) beamforming and the adaptive beamforming data at (a) 5 kHz and (b) 7.5 kHz.

beamforming method can help DAMAS to attain a convergent solution with a smaller number of iterations (12 iterations for the adaptive beamforming data compared to 31 iterations for the conventional beamforming data). The convergence curves are more similar at 7.5 kHz, compared to the curves at 5 kHz, because the conventional beamformer has side lobes of small amplitudes at high frequency. Although the convergence performance is not as distinctive as that of the lower frequency case, the adaptive beamforming method still reduces the DAMAS computation time by almost 60%.

The convergent mean-squared values (after 30,000 DAMAS iterations) at frequency ranges between 1.5 and 7.5 kHz are shown in Fig. 12, where the DAMAS solutions of the adaptive beamforming data computed with various  $\lambda$  are compared to the DAMAS solution of the conventional delay-and-sum beamforming data. It can be seen that the DAMAS results of the conventional beamforming data agree well with those of the adaptive beamforming data when  $\lambda=0.5$ . The difference is about 1.8 dB at 2.5 kHz, and is reduced along with the increase of the frequency. The difference is less than

0.2 dB beyond 5 kHz. On the other hand, the DAMAS results of the adaptive beamforming data with  $\lambda=0.1$  are 5–6 dB lower, although a similar spectral shape is maintained. The deviation is too large (bigger than the empirically set threshold: 3 dB) and the  $\lambda=0.1$  setup is thus recognized as inappropriate. The DAMAS computation has also been conducted for the classical adaptive beamforming data without diagonal loading, i.e.,  $\lambda=0$ . It can be seen that both the profile shape and the amplitudes are quite aberrant, which reflects the fact again that adaptive beamforming without diagonal loading is unsuitable for practical experiments.

## V. SUMMARY

In this work an adaptive beamforming algorithm has been proposed for aeroacoustic applications. This algorithm is applied to experimental aeroacoustic data and the acoustic image results are compared to that of the conventional beamforming method. It can be seen that the adaptive beamforming algorithm does not produce an acoustic image with significant improvement in resolution. The possible reasons include: (a) The adaptive beamforming is optimized for a rank-one signal model,<sup>29</sup> whereas the practical data contains many discrete (and possibly correlated) noise sources distributed in a region;<sup>13</sup> (b) the passage of sound waves through the open jet shear layer affects the coherence between microphone measurements; and (c) the noise model adopted in adaptive beamformer may be inconsistent with practical cases.

Few results for practical experimental data can be found in literature. This work develops an adaptive beamforming algorithm specifically for aeroacoustic tests and applies it to the practical data in an effort to fill this gap. The algorithm is applied to experimental data acquired in an anechoic chamber facility. The present results from practical experimental data suggest that the adaptive beamforming method could not produce an acoustic image with a significant improvement in resolution. However, deconvolution post-processing for adaptive beamforming results can be enhanced compared to that for conventional beamforming results. For example, the adaptive beamforming method is able to reduce the DAMAS computation time by at least 60% for the practical case considered in this work. Hence, it is still advantageous to consider the adaptive beamforming method in aeroacoustic measurements.

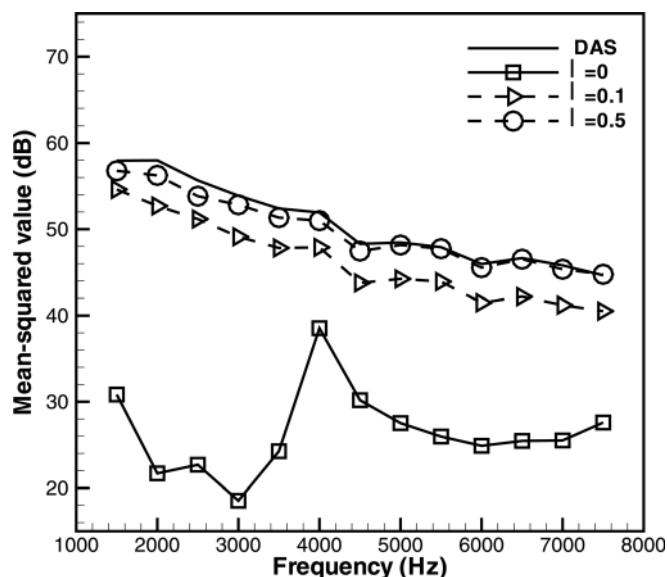


FIG. 12. The convergent mean-squared values for the DAMAS results of the conventional delay-and-sum (DAS) beamforming and the adaptive beamforming data at frequencies range between 1.5 and 7.5 kHz.

## ACKNOWLEDGMENTS

The majority of this research was supported by the National Science Foundation grant of China (Grant Nos. 11172007, 11050110109, and 11110072). The experiments were conducted at ISVR, University of Southampton. We acknowledge Professor Xin Zhang for his support in the experiments.

- <sup>1</sup>D. R. Morgan and T. M. Smith, "Coherence effects on the detection performance of quadratic array processors, with applications to large-array matched-field beamforming," *J. Acoust. Soc. Am.* **87**, 737–747 (1990).
- <sup>2</sup>D. E. Dudgeon, "Fundamentals of digital array processing," *Proc. IEEE* **65**, 898–904 (1977).
- <sup>3</sup>Y. Liu, A. R. Quayle, A. P. Dowling, and P. Sijtsma, "Beamforming correction for dipole measurement using two-dimensional microphone arrays," *J. Acoust. Soc. Am.* **124**, 182–191 (2008).
- <sup>4</sup>H. C. Shin, W. R. Graham, P. Sijtsma, C. Andreou, and A. C. Faszer, "Implementation of a Phased Microphone array in a closed-section wind tunnel," *AIAA J.* **45**, 2897–2909 (2007).
- <sup>5</sup>R. A. Gramann and J. W. Mocio, "Aeroacoustic measurements in wind tunnels using adaptive beamforming methods," *J. Acoust. Soc. Am.* **97**, 3694–3701 (1995).
- <sup>6</sup>X. Huang, S. Chan, X. Zhang, and S. Gabriel, "Variable structure model for flow-induced tonal noise control with plasma actuators," *AIAA J.* **46**, 241–250 (2008).
- <sup>7</sup>X. X. Chen, X. Huang, and X. Zhang, "Sound radiation from a bypass duct with bifurcations," *AIAA J.* **47**, 429–436 (2009).
- <sup>8</sup>M. J. Lighthill, "On sound generated aerodynamically. I. General theory," *Proc. R. Soc. London Ser. A* **221**, 564–587 (1952).
- <sup>9</sup>P. T. Soderman and C. S. Allen, "Microphone measurements in and out of stream," in *Aeroacoustic Measurements*, edited by T. J. E. Mueller (Springer, New York, 2002), Chap. 1, pp. 26–41.
- <sup>10</sup>B. D. Van Veen and K. M. Buckley, "Beamforming: A versatile approach to spatial filtering," *IEEE ASSP Mag.* **5**, 4–24 (1988).
- <sup>11</sup>M. C. Remillieux, E. D. Crede, H. E. Camargo, R. A. Burdisso, W. J. Devenport, M. Rasnick, P. V. Seeters, and A. Chou, "Calibration and demonstration of the new Virginia Tech anechoic wind tunnel," 14th AIAA/CEAS Aeroacoustics Conference and 29th AIAA Aeroacoustics Conference, Vancouver, May 2008, AIAA Paper No. 2008-2911.
- <sup>12</sup>E. Sarraj, C. Fritzsche, T. Geyer, and J. Giesler, "Acoustic and aerodynamic design and characterization of a small-scale aeroacoustic wind tunnel," *Appl. Acoust.* **70**, 1073–1080 (2009).
- <sup>13</sup>X. Huang, "Real-time algorithm for acoustic imaging with a microphone array," *J. Acoust. Soc. Am.* **125**, EL190–EL195 (2009).
- <sup>14</sup>X. Huang, I. Vinogradov, L. Bai, and J. C. Ji, "Observer for phased microphone array signal processing with nonlinear output," *AIAA J.* **48**, 2702–2705 (2010).
- <sup>15</sup>L. Bai and X. Huang, "Observer-based beamforming algorithm for acoustic array signal processing," *J. Acoust. Soc. Am.* **130**, 3803–3811 (2011).
- <sup>16</sup>Y. W. Wang, J. Li, P. Stoica, M. Sheplak, and T. Nishida, "Wideband RELAX and wideband CLEAN for aeroacoustic imaging," *J. Acoust. Soc. Am.* **115**, 757–767 (2004).
- <sup>17</sup>T. F. Brooks and W. M. Humphrey, "A deconvolution approach for the mapping of acoustic sources (DAMAS) determined from phased microphone arrays," *J. Sound Vib.* **294**, 858–879 (2006).
- <sup>18</sup>P. Sijtsma, "CLEAN based on spatial source coherence," *Int. J. Aeroacoust.* **6**, 357–374 (2007).
- <sup>19</sup>T. Yardibi, J. Li, P. Stoica, and L. N. Cattafesta, "Sparsity constrained deconvolution approaches for correlated acoustic source mapping," *J. Acoust. Soc. Am.* **123**, 2631–2642 (2008).
- <sup>20</sup>P. A. Ravetta, R. A. Burdisso, and W. F. Ng, "Noise source localization and optimization of phased-array results," *AIAA J.* **47**, 2520–2533 (2009).
- <sup>21</sup>T. Yardibi, J. Li, P. Stoica, N. S. Zawodny, and L. N. Cattafesta III, "A covariance fitting approach for correlated acoustic source mapping," *J. Acoust. Soc. Am.* **127**, 2920–2931 (2010).
- <sup>22</sup>O. L. Frost, "An algorithm for linearly constrained adaptive array processing," *Proc. IEEE* **60**, 926–935 (1972).
- <sup>23</sup>P. Stoica, Z. S. Wang, and J. Li, "Robust Capon beamforming," *IEEE Signal Proc. Lett.* **10**, 172–175 (2003).
- <sup>24</sup>H. Cox, R. M. Zeskind, and M. M. Owen, "Robust adaptive beamforming," *IEEE Trans. Acoust. Speech. Sig. Proc.* **ASSP-35**, 1365–1376 (1987).
- <sup>25</sup>Z. S. Wang, J. Li, P. Stoica, T. Nishida, and M. Sheplak, "Constant-beamwidth and constant-powerwidth wideband robust Capon beamformers for acoustic imaging," *J. Acoust. Soc. Am.* **116**, 1621–1631 (2004).
- <sup>26</sup>Y. T. Cho and M. J. Roan, "Adaptive near-field beamforming techniques for sound source imaging," *J. Acoust. Soc. Am.* **125**, 944–957 (2009).
- <sup>27</sup>L. Bai and X. Huang, "Observer-Based Method in Acoustic Array Signal Processing," *16th AIAA/CEAS Aeroacoustics Conference and 31st AIAA Aeroacoustics Conference*, Stockholm, May 2010, AIAA Paper No. 2010-3813.
- <sup>28</sup>X. Huang, "Real-time location of coherent sound sources by the observer-based array algorithm" *Meas. Sci. Technol.* **22**, 065501 (2011).
- <sup>29</sup>S. Shahbazpanahi, A. B. Gershman, Z. Q. Luo, and K. M. Wong, "Robust adaptive beamforming for general-rank signal models," *IEEE Trans. Signal Process.* **51**, 2257–2269 (2003).
- <sup>30</sup>R. G. Lorenz and S. P. Boyd, "Robust minimum variance beamforming," *IEEE Trans. Signal Process.* **53**, 1684–1696 (2005).
- <sup>31</sup>X. Huang, X. Zhang, and Y. Li, "Broadband flow-induced sound control using plasma actuators," *J. Sound Vib.* **329**, 2477–2489 (2010).
- <sup>32</sup>X. Huang and X. Zhang, "The Fourier pseudospectral time-domain method for some computational aeroacoustics problems," *Int. J. Aeroacoust.* **5**, 279–294 (2006).